2.2 TEM CHARACTERIZATION OF 14YWT AND 12YWT ODS FERRITIC ALLOYS NEUTRON IRRADIATED AT 500°C USING IN-SITU HELIUM INJECTION - H.J. Jung, D. J. Edwards, R. J. Kurtz (Pacific Northwest National Laboratory), G. R. Odette, Y. Wu, T. Yamamoto (University of California Santa Barbara)

OBJECTIVE

The objective is to characterize the microstructure and chemical evolution in two oxide dispersion strengthened (ODS) ferritic alloys, 14YWT and 12YWT, containing 14 and 12 Cr wt % respectively, irradiated with neutrons to 21.2 dpa at 500°C. Samples were injected with 1230 appm of helium via an in situ He injection (ISHI) technique.

SUMMARY

This report summaries TEM characterization of 14YWT and 12YWT, ODS ferritic alloys with 14 and 12 wt % Cr, respectively, to compare the effect of neutron irradiation with and without concurrent He injection using in situ He injection. The density and average size of <100>/{100} type dislocation loops are always larger than those of 1/2<111>/{111} type, but this difference is significantly affected by He implantation. The density of dislocation loops of both types ranges from ~1 to $4x10^{21}$ m^{-3} with average size ranging from 5~20 nm. 14YWT has lower density but larger size dislocation loops than 12YWT, while the line dislocation density of 14YWT is 3 times lower than that of 12YWT. Helium bubble densities of both 14YWT and 12YWT are $1.9x10^{23}$ m^{-3}, the average He bubbles size of 14YWT and 12YWT are 1.4 and 1.2 nm, respectively. 14YWT exhibits α-α' phase separation, Y-rich particles and uniformly distributed W. In addition to those features, 12YWT exhibits Y-Ti-O particles (not Y-O rich) and elongated Cr-rich phases.

PROGRESS AND STATUS

Introduction

Oxide-dispersed strengthened (ODS) alloys provide excellent high-temperature mechanical properties with high swelling-resistance for first-wall materials for future fusion reactors [1,2]. The materials for the first wall will inescapably endure a severe thermal and neutron-irradiation environment, with the presence of high levels of He production (10 appm He per dpa) from transmutation creating an even more challenging environment [3]. The high levels of He impacts the mechanical properties of ferritic alloys through He embrittlement and the formation of He bubbles and voids in the matrix, at lath boundaries, grain boundaries, and at particle-matrix interfaces [4], which can lower the high-temperature tensile and creep properties. A further consequence of the He accumulation is that the small bubbles (d<2 nm) can increase in size and convert to large unstably growing voids, thereby causing significant swelling [5]. In order to prevent the transition of He bubbles to voids, microstructures are being designed to provide a high density of nanoscale trapping sites such as nano-size oxide particles to broadly disperse He gas atoms [1] so that bubbles do not reach the critical size. We are currently examining the effectiveness of oxide dispersions, as well as elucidating the mechanisms of He movement, trapping, and interaction with various defects and interfaces in ferritic alloys under irradiation.

Due to practical difficulties in realizing material performance under a fusion-relevant irradiation environment, the in-situ He injection (IHSI) technique has been developed to explore the effects of simultaneous neutron irradiation and He injection on microstructural evolution of candidate materials, as detailed in the literature [7]. Here we present analytical transmission electron microscopy (TEM) characterization of neutron-irradiated and He/neutron-irradiated effects on 14YWT and 12YWT ferritic alloys with a nominally 4 µm thick NiAl layer deposited to one surface. When irradiated with neutrons, the ^{59}Ni isotope undergoes a ^{59}Ni (n, α) reaction and injects some fraction of the energetic He into the ferritic alloy. The samples were irradiated to a dose of 21.2 dpa at 500°C in the JP-27 experiment in the HFIR reactor for several operating cycles over a span of years, leading to an estimated 1230 appm of He in the sample over a uniform depth of about 6 µm. Cross-sectional TEM samples were prepared by the focus

ion beam (FIB) technique to characterize microstructure related features such as He bubbles/voids, dislocation loops/line dislocations, and oxide or carbide particles.

Experimental Procedure

The compositions of the 14YWT and 12YWT ODS alloys in this report are listed in Table 1. Both 14YWT and 12YWT are powder metallurgy products, but 14YWT was hot isostatically pressed at 1150°C and 12YWT was hot extruded at 1150°C. All samples were neutron irradiated to a dose of 21.2 dpa at 500°C in the High Flux Isotope Reactor (HFIR) at Oak Ridge National Laboratory (ORNL). A 4 µm NiAl coating used for the ISHI was applied to one side of a 3-mm TEM disc, which allows a FIB lamella to be extracted from either side of the TEM discs to explore the impact of neutron irradiation with or without concurrent helium injection. The NiAl coating produces a He concentration of about 1230 appm in the ferritic matrix extending to a depth of ~6 µm below the coating. Cross-sectional TEM samples, prepared by a FIB (FEI Quanta 3D), were finalized with low-energy surface cleaning (2 keV Ga^+ ion) at ±2° tilt angles. The TEM lamellae were extracted from each side of the TEM disc.

Table 1. Composition of examined ODS alloys

Alloy	Composition (wt.%) with Fe balance											
	Cr	Y(Y2O3)	W	Ti	Al	Mg	Si	V	Mo	Mn	Re	Os
14YWT	13.76	0.13	2.04	0.41	0.82	0.09	0.22	0.24	0.07	2.16	0.21	0.54
12YWT	11.98	0.15	1.74	0.35	0.84	0.17	0.14	0.21	0.32	2.10	0.15	0.49

The analytical TEM characterization was performed using a newly installed Cs-corrected JEOL ARM 200cF microscope equipped with various detectors, including a Centurio silicon drift detector (SDD) for energy dispersive X-ray spectroscopy (EDS), a Gatan Quantum 965 Dual EELS system, and high angle annular dark field (HAADF) and bright field (BF) STEM detectors. This instrument can produce a Cs-corrected sub-Å STEM probe with high electron current because of the cold field emission gun (CFEG), allowing enhanced spatial resolution of EDS mapping over shorter times. TEM sample thickness was determined through convergent-beam electron diffraction (CBED). Bright-field TEM (BFTEM) images of He bubbles and voids were acquired using an over/under-focus technique, and measured bubble sizes are about 87% of the actual bubble size at an under-defocus of 750 nm as determined from a previous modeling study [7,8]. The dislocation loops and line dislocations were imaged using a specific diffraction vector of g=200 at two-beam conditions near a 001 zone axis in bcc matrix [9].

Results and Discussion

First, the effect of neutron-irradiation at 500°C with and without helium injection on dislocation loops and line dislocations of 14YWT and 12YWT was investigated from BFTEM images (Fig. 1a~d) taken from a slightly weak two-beam condition to g=200 direction near a 001 zone axis in bcc matrix. Density and size measurements of <100>/{100} and 1/2<111>/{111} type loops, examples of which are shown in Fig. 1e and 1f, show that the injection of He under neutron increases the density and size of each dislocation loop type compared to those measured in the neutron-only irradiated side of the disc, while line dislocation densities are almost same in 14YWT and 12YWT (slightly lowered though by He injection). Interestingly, the density and average size of <100>/{100} loops are always larger than those of 1/2<111>/{111} loops irrespective of the presence of helium, leading to the question of why <100>/{100} loops are more dominant. Careful long-term simulation of the nucleation, growth and mobility of each type loop is needed to elucidate this phenomenon, requiring careful consideration of several factors such as physical distribution of ODS particles, the role of grain boundaries and pre-existing dislocation sinks, chemical changes in the microstructure like α-α' phase separation, second phase formation, and segregation of certain elements (ex. Cr, Ti). The density range of each dislocation loop is roughly 1 to $4x10^{21}$ m^{-3} with average size ranging from 5~20 nm. 14YWT has lower density but larger size dislocation loops than those in 12YWT under the same conditions, while line dislocation density of 14YWT is about 3 times lower than that of 12YWT.

Interestingly, size distribution histograms of <100>/{100} and 1/2<111>/{111} loops in Fig. 2 provide detailed data on how loops grow under the influence of He. Please note that the histograms have the

same population scale (Y-axis) to facilitate a comparison between histograms from the neutron-only irradiated side (left) versus histograms for the loops on the He-injected side (right). While the neutron-only irradiated cases of each type of loop usually have one dominant peak at a small size, the dual He/neutron-irradiation cases display bimodal histograms with a broader distribution at larger sizes (> 30 nm). It is significant that in the 14YWT alloy the densities of the <100>/{100} loops are higher and the loops extend to larger sizes compared to the 1/2<111>/{111} loops under He injection. The loop characteristics suggest that the histogram shapes are fairly similar when comparing the two alloys, however, 12YWT in general has a higher density of smaller loops. The reasons for this are not presently understood.

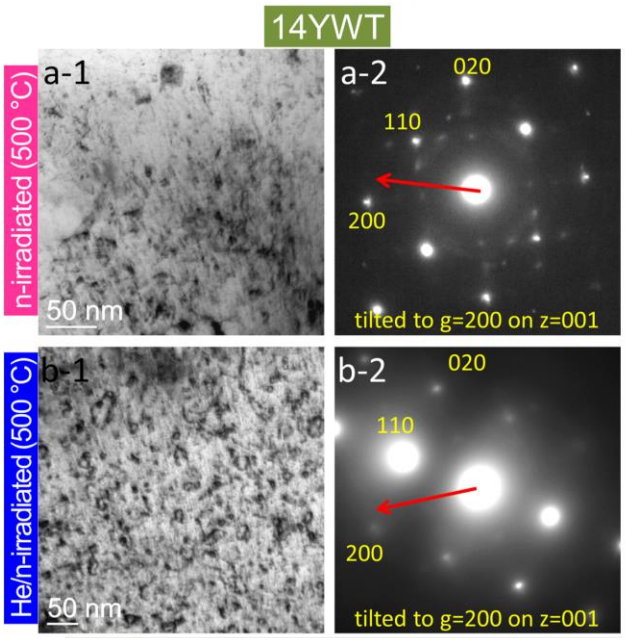

e

14YWT	Dislocation Loops				Line Dislocations
	<100>/{100} type		½<111>/{111} type		
	density [10^{21}/m^3]	size (stdev) [nm]	density [10^{21}/m^3]	size (stdev) [nm]	density [10^{13}/m^3]
n	1.8	11.2 (7.1)	1.5	8.9 (6.6)	6.3
He/n	3.6	17.1 (11.2)	1.8	16.4 (9.2)	5.6

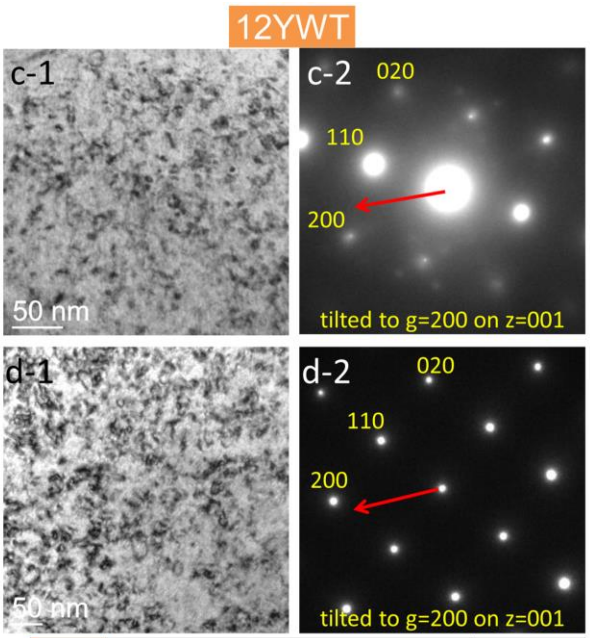

f

12YWT	Dislocation Loops				Line Dislocations
	<100>/{100} type		½<111>/{111} type		
	density [10^{21}/m^3]	size (stdev) [nm]	density [10^{21}/m^3]	size (stdev) [nm]	density [10^{13}/m^3]
n	2.9	6.1 (2.8)	2.0	6.9 (3.7)	18
He/n	3.3	14.5 (8.8)	2.8	10.5 (3.8)	17

Figure 1. Dislocation loops and line dislocations of 14YWT (a and b) and 12YWT (c and d) under neutron-irradiation and He/neutron-irradiation at 500 °C from four sets of BFTEM images (left) and SAD patterns (right) and statistics (e and f) of <100>/{100} and 1/2<111>/{111} type loops and line dislocations measured from 3 different images of each sample. Please note that each BFTEM (denoted as 1) was taken from each diffraction condition (denoted as 2), which is a slightly weak g=200 two-beam condition near the 001 zone axis of bcc matrix to show better diffraction contrast of dislocations. Interestingly, the density and size of <100>/{100} and 1/2<111>/{111} dislocation loops in both 14YWT and 12YWT increase under irradiation from only neutron to dual He and neutron, while line dislocation densities are similar.

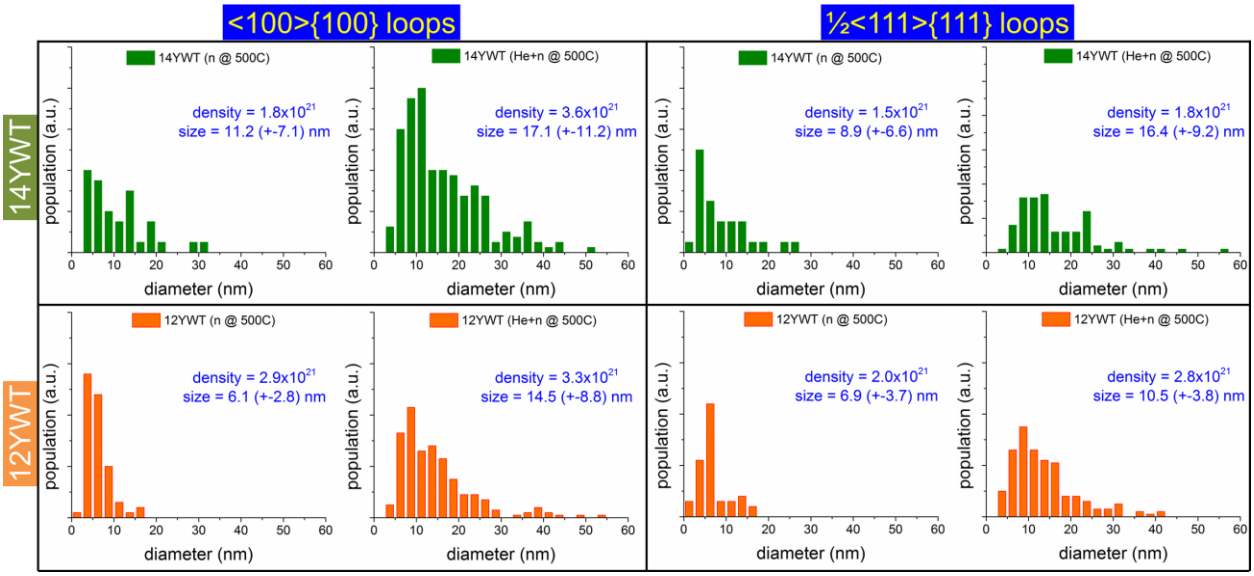

Figure 2. Histograms of <100>/{100} and 1/2<111>/{111} loop sizes in 14YWT (top green) and 12YWT (bottoms orange) under only neutron-irradiation (left) and He/neutron-irradiation (right) at 500 °C.

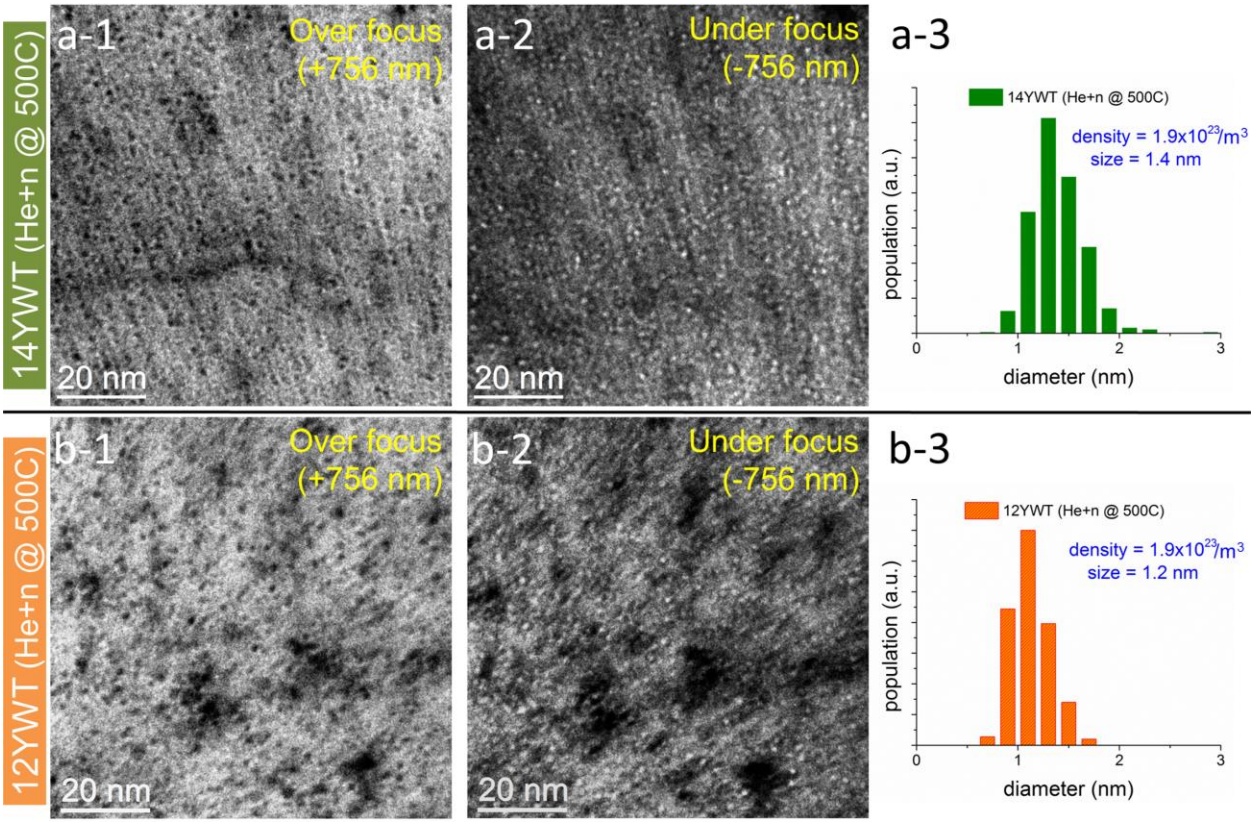

Figure 3. Two sets of BFTEM images at over-focus (denoted as 1 at right) and under-focus (denoted as 2 at left) of the He/neutron-injected side of 14YWT (a) and 12YWT (b) with summary histograms of He bubbles in matrix. Please note that He bubble densities of 14YWT and 12YWT are similar at 1.9×10^{23} m^{-3} and average He bubble size of 12YWT is slightly smaller than 14YWT by ~0.2 nm, as confirmed by the histogram peak positions.

Second, we examined small He bubbles in the matrix of the He-implanted sides as can be seen in Fig. 3. A notable observation is that the matrix of both 14YWT and 12YWT contain only very small He bubbles (d < 2 nm) without any larger voids unlike 14YW and F82H-mod.3 [10]. From a direct comparison of 14YW with 14YWT and 12YWT under the same irradiation environment, it can be deduced that Ti has an important role in keeping He dispersed into small bubbles via refinement of the oxide particles that serve as effective traps for helium. He bubble densities of both 14YWT and 12YWT are the same at 1.9×10^{23} m^{-3}, but the average He bubble size in the 12YWT is slightly smaller than that of 14YWT (1.2 nm versus 1.4 nm, respectively). It is unclear if the chemical changes in the matrix have any direct, measureable effect on the helium distribution.

In order to identify the particle type (or composition) and explore chemical evolution during irradiation, STEM-EDS elemental maps of Fe, Cr, C, W, Y, T, and O with a comparable set of BF/HAADF STEM images at various magnifications were taken, the results are presented in Figs. 4 & 5. In the case of He/neutron-irradiated 14YWT, Fig. 4-a presents an overview of large particle (50~200 nm) distributed predominantly on grain boundaries; these are Ti-rich particles. While only a few large particles (50~200 nm) are observed inside grains, an unusual Cr-Ti-rich particle is found. At low magnification, Y-rich particles are not clearly detected, and W is distributed evenly throughout the matrix without significant segregation. Interestingly, an intermediate magnification of elemental mapping in Fig. 4b displays distinctive Cr-segregation along a grain boundary passing through a large Ti-rich particle and obvious phase separation of α (Fe-rich) and α' (Cr-rich). Observed Y-O particles and Cr-rich phases tend to segregate to Ti-rich particles located at grain boundaries. Preferential chemical binding of Cr-C and Y-O is observed, while W is independently distributed.

In case of neutron-irradiated 12YWT, Fig. 5a and 5b at low and intermediated magnification maps show Y-Ti-O particles, elongated Cr-rich phases (probably chromium carbide) and phase separation of α (Fe-rich) and α' (Cr-rich) with spherical morphologies. A higher magnification map in Fig. 5c shows that Y-Ti-O particles are attached to Cr-rich phases, suggesting a tendency for Cr segregation toward these particles. W is distributed uniformly as in the case of 14YWT regardless of other present in 12YWT. Y-Ti-O particles are observed in the EDS maps ranging roughly in size from 5~70 nm. Fine Y-rich particles (< 5 nm) should be clearly observed in a much thinner TEM sample (10~20 nm thick) in STEM-EDS/EELS mapping and high-resolution S/TEM images to investigate the role of Ti.

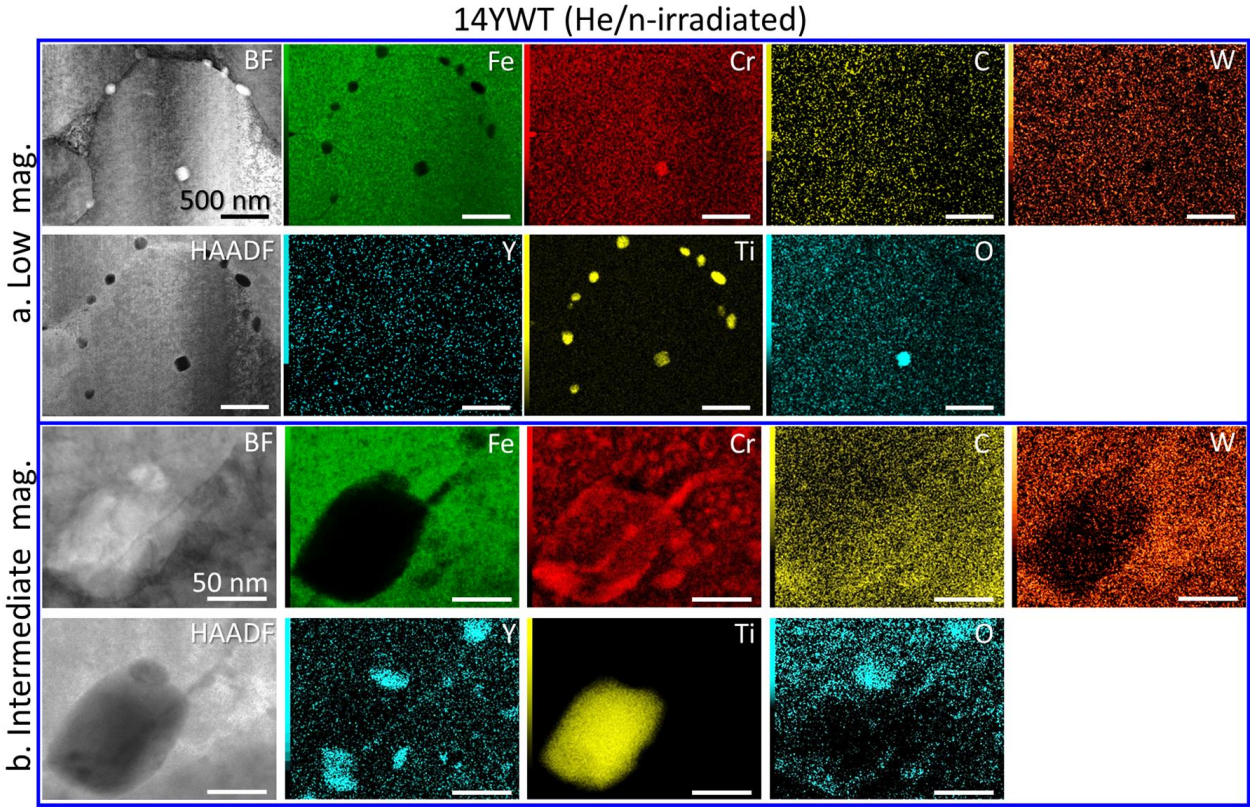

Figure 4. STEM-EDS maps of He/neutron-irradiated 14YWT at 500 °C at low (a) and intermediate (b) magnifications composed of BF and HAADF STEM images and elemental maps of Fe, Cr, C, W, Y, T, and O. (a) Low magnification map shows Ti-rich particles dominantly are located at grain boundaries, and unusual Cr-Ti segregation. Low magnification does not have enough resolution to show small Y-rich particles. (b) Intermediate magnification shows Cr-segregation along a grain boundary crossing a large Ti-rich particle (yellow) and also clear phase separation of α (Fe-rich) and α' (Cr-rich). Y-O particles and Cr-rich phases tend to segregate to the Ti-rich particles. Preferential chemical associations of Cr-C and Y-O are observed, while W is uniformly distributed. Please note that Y-Ti-O nano-oxide particles are not directly observed in this 14YWT, however it has very small He bubble (d_{ave}=~1.4 nm) with a density of 1.9×10^{23} m^{-3} similar to 12YWT. Care must be taken in interpreting the oxygen map because of overlap between the O K_α peak overlapping with the Cr L_α peaks.

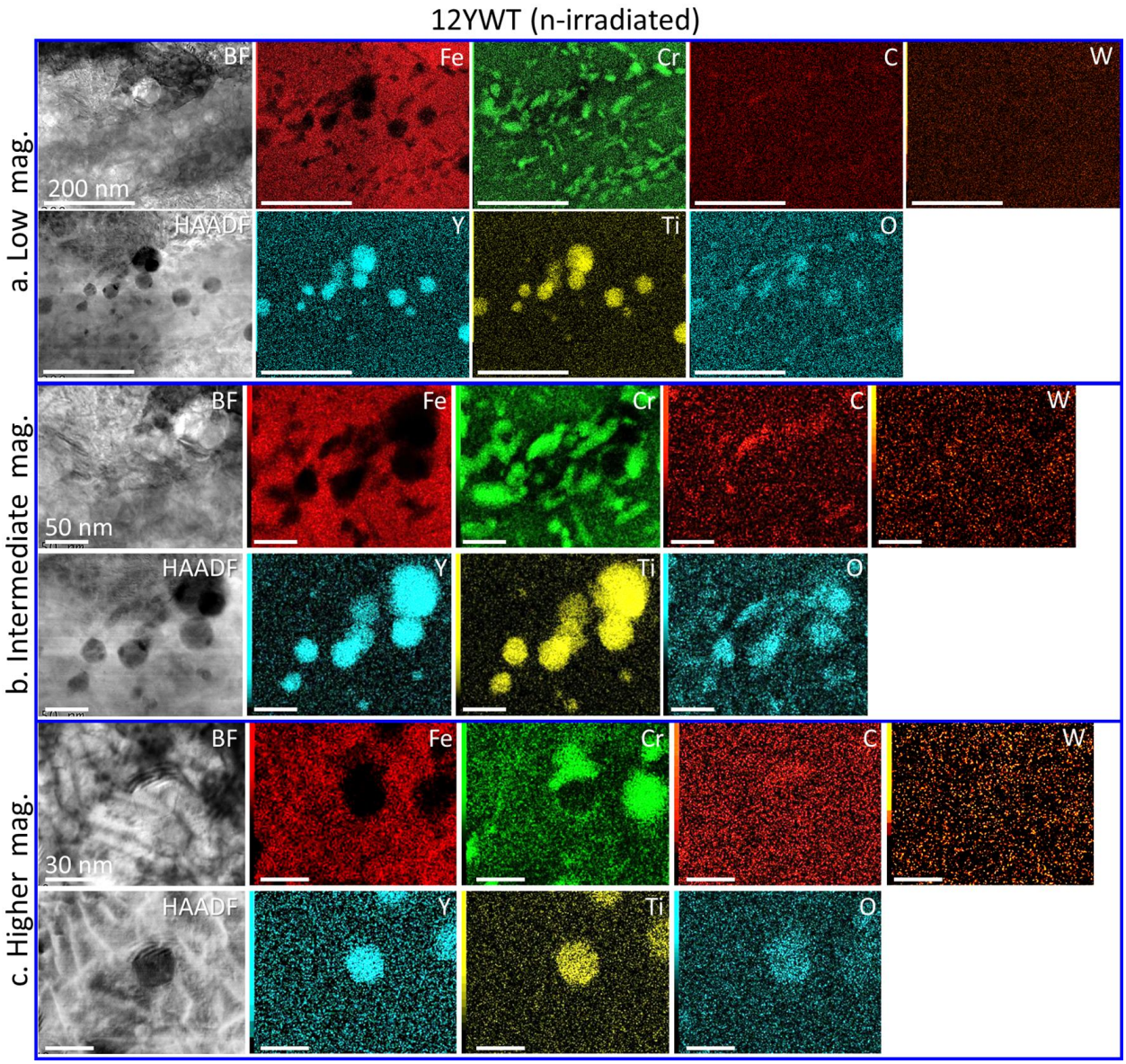

Figure 5. STEM-EDS maps of neutron-irradiated 12YWT at 500 °C at low (a), intermediate (b) and higher (c) magnifications composed of BF and HAADF STEM images and elemental maps of Fe, Cr, C, W, Y, T, and O. Low and intermediated magnification maps (a and b) show Y-Ti-O particles unlike 14YWT and clear elongated Cr-rich phases (probably Chromium carbide) and phase separation of α(Fe-rich) and α' (Cr-rich) with spherical shape. Higher magnification map (c) displays Y-Ti-O particles are attached to Cr-rich phases, inferring that Cr preferentially segregates to these particles, more precisely Y-rich particles considering the 14YWT case. W is uniformly distributed.

Acknowledgements

This research was supported by the U. S. Department of Energy, Office of Fusion Energy Sciences, under contract DE-AC06-76RLO1830. A portion of the research was performed using EMSL, a national scientific user facility sponsored by the DOE's Office of Biological and Environmental Research and located at PNNL.

References

[1] G.R. Odette, M.J. Alinger, and B.D. Wirth, Annu. Rev. Mater. Res. 38 (2008) 471.

[2] R.J. Kurtz, A. Alamo, E. Lucon, Q. Huang, S. Jitsukawa, A. Kimura, R.L. Klueh, G.R. Odette, C. Petersen, M.A. Sokolov, P. Spätig, J.W. Rensman, J. Nucl. Mater. 386-388 (2009) 411.

[3] N. Baluc, K. Abe, J.L. Boutard, V.M. Chernov, E. Diegele, S. Jitsukawa, A. Kimura, R.L. Klueh, A. Kohyama, R.J. Kurtz, R. Lässer, H. Matsui, A. MÖslang, T. Muroga, G.R. Odette, M.Q. Tran, B. van der Schaaf, Y. Wu, J. Yu, and S.J. Zinkle, Nucl. Fusion 47 (2007) S696.

[4] H. Ullmaier, Nuclear Fusion. 24 (1984) 1039.

[5] R.E. Stoller, G.R. Odette, J. Nucl. Mater. 131 (1985) 118.

[6] R. Schäeublin, Y.L. Chiu, J. Nucl. Mater. 362 (2007) 152.

[7] B. Yao, D. J. Edwards, R. J. Kurtz, G. R. Odette, and T. Yamamoto, Fusion Reactor Materials Program 51 (2011), 85.

[8] B. Yao, D. J. Edwards, R. J. Kurtz, G. R. Odette, and T. Yamamoto, J. Electron Microsc. 61(6) (2012) 393.

[9] B. Yao, D. J. Edwards, and R. J. Kurtz, J. Nucl. Mater. 434 (2012) 402.

[10] H.J. Jung, D. J. Edwards, B. Yao, R. J. Kurtz, G. R. Odette, T. Yamamoto , Fusion Reactor Materials Program 56 (2014) 19.